[1.]László Péter KISS

THE EFFECT OF MATERIAL COMPOSITION ON THE STABILITY OF BI-LAYERED ARCHES WITH RECTANGULAR CROSS-SECTION

[1.]Institute of Applied Mechanics, University of Miskolc, Miskolc, HUNGARY

Abstract: This article investigates how the material composition can affect the in-plane stability of circular arches with bi-layered rectangular cross-section. The Euler-Bernoulli beam theory is used. The materials are linearly elastic and isotropic. The one dimensional mechanical model is geometrically nonlinear: moderately large rotations are assumed. The end-supports are ideal pins and out-of plane displacements are restricted. The loading is a concentrated force at the crown. Evaluations are carried out graphically. It is found that not only the geometry but the material distribution has considerable effects on the critical load.
Keywords: nonlinear stability, circular arch, bi-layered, buckling

1. INTRODUCTION

Curved structural and machine elements have various engineering applications [1,2,3]. Arches are commonly used in engineering structures because of their favourable load carrying capabilities. As buckling is a common way of failure, it has been the subject of investigations for quite a while. It is known that the mechanical behaviour of shallow circular arches is strongly nonlinear. In recent years, many novel mechanical models have been introduced like [3,4] by Bradford et al. These articles investigate the in-plane static behaviour of such structural elements with uniform cross-section using a one-dimensional beam model. Recent relevant results for non-uniform members were published e.g., in [5,6] by Jin et al. There are also available results for nonhomogeneous materials by Bateni et al [7,8].

In the current article, based on [9-11], it is demonstrated how the material composition affects the critical (buckling) load of bi-layered uniform shallow circular arches made of linearly elastic and isotopic materials. The mechanical model is geometrically nonlinear, using the *single-layer Euler-Bernoulli beam theory. Moderately large rotations are assumed.* The arch is pinned at both ends and the loading is a constant concentrated force applied at the crown point.

2. KINEMATICS

Figure 1 shows a portion of the arch; the orthogonal curvilinear coordinate system $(\xi\eta\zeta)$ is attached to the centroidal axis with radius ρ_o and the unit vectors are $\mathbf{e}_\xi$, $\mathbf{e}_\eta$ and $\mathbf{e}_\zeta$. The cross-section of the arch is uniform and symmetric to the axis ζ. On the centroidal axis, the E-weighted first moment of the cross-section to η is zero. The Young modulus E can depend on ζ. The arc coordinate s is measured from the crown point while $\varphi = s/\rho_o$ is the angle coordinate. The included angle of the arch is 2ϑ.

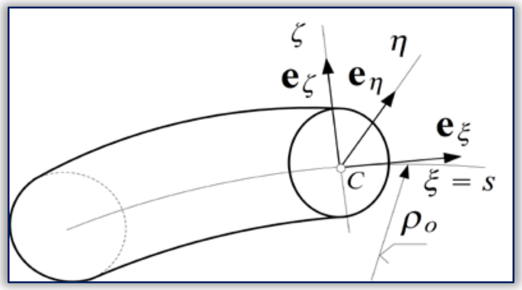

Figure 1: The arch and its centroidal axis

The mechanical model is based on the single-layer Euler-Bernoulli beam theory. Just as in [3,9], it considers small axial strains $(\varepsilon_{o\xi})$ and moderately large rotations ($\psi_{o\eta}$) as

$$\psi_{o\eta} = -\frac{dw_o}{ds} + \frac{u_o}{ds}, \varepsilon_{o\xi} = \frac{du_o}{ds} + \frac{w_o}{\rho_o}; \ \varepsilon_m = \varepsilon_{o\xi} + \frac{1}{2}\psi_{o\eta}^2 \tag{1}$$

with $\varepsilon_m; u_o; w_o$ being the membrane strain and the pre-buckling displacements of the centroidal axis in the tangential/normal direction.

Recalling the Hooke law, the axial force (N) and bending moment (M) are given by [9]

$$M = \int_A E\varepsilon_\xi \zeta dA = -I_{e\eta}\left(w_o^{(2)} + w_o\right)/\rho_o^2, N = \int_A E\varepsilon_\xi dA = A_e\varepsilon_m - I_{e\eta}\kappa_o/\rho_o \tag{2}$$

with the notations

$$A_e = \int_A E dA; \quad I_{e\eta} = \int_A E\zeta^2 dA, \tag{3}$$

$$\rho_o^n d^n(\ldots)/ds^n = d^n(\ldots)/d\varphi^n = (\ldots)^{(n)}, \ n = 1,2,\ldots; \ m = A_e\rho_o^2/I_{e\eta}. \tag{4}$$

After buckling, the increments are denoted by subscript $(\ldots)_b$, therefore, similarly as beforehand, the typical quantities are

$$\psi_{o\eta b} = u_{ob}/\rho_o - dw_{ob}/ds; \ \varepsilon_{o\xi b} = \frac{du_{ob}}{ds} + \frac{w_{ob}}{\rho_o}; \ \varepsilon_{mb} = \varepsilon_{o\xi b} + \psi_{o\eta}\psi_{o\eta b} \tag{5}$$

$$M_b = -I_{e\eta}\left(w_{ob}^{(2)} + w_{ob}\right)/\rho_o^2 \quad \text{and} \quad N_b = A_e\varepsilon_{mb} - M_b/\rho_o \,. \tag{6}$$

3. EQUILIBRIUM EQUATIONS

Altogether, three equilibrium states are distinguished: the initial, the pre-buckling (the effect of the load on the initial shape is accounted not to overestimate the critical load) and the post-buckling state. Figure 2 shows the centroidal axis of the arch in the initial configuration (continuous line) and in the pre-buckling equilibrium state (dashed line) assuming symmetric support and loading conditions. Using a generalized approach, at this point, the arch is rotationally restrained at the ends with torsional springs whose spring constants are $k_{\gamma\ell}$, $k_{\gamma r}$ and the loading consists of the distributed forces $\mathbf{f} = f_n\mathbf{e}_\zeta + f_t\mathbf{e}_\xi$ and the concentrated force $P_\zeta(\varphi = 0)$.

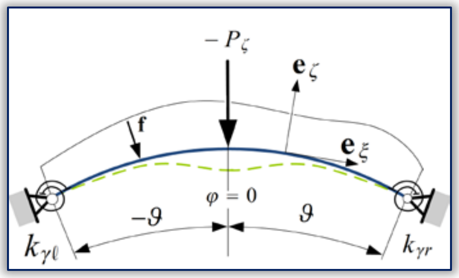

Figure 2: One dimensional model

Using the principle of virtual work, it is found that the pre-buckling equilibrium is governed by equations [9]

$$\frac{dN}{ds} + \frac{1}{\rho_o}\left[\frac{dM}{ds} - \left(N + \frac{M}{\rho_o}\right)\psi_{o\eta}\right] = 0, \quad \frac{d}{ds}\left[\frac{dM}{ds} - \left(N + \frac{M}{\rho_o}\right)\psi_{o\eta}\right] - \frac{N}{\rho_o} = 0, \tag{7}$$

In the sequel, some terms are dropped, i.e., $f_n = f_t = k_{\gamma\ell} = k_{\gamma_r} = 0$. So the pinned-pinned arch is subject to a concentrated load only. Recalling relations (1)-(3), the above equilibrium equations become

$$\varepsilon_m = \text{constant}\,, \tag{8}$$

$$W_o^{(4)} + \left(2 + \chi^2 - 1\right)W_o^{(2)} + \chi^2 W_o = \chi^2 - 1, \quad W_o = w_o/\rho_o, \quad \chi^2 = 1 - m\varepsilon_m \tag{9}$$

which are comparable to the equations published in [4]. The post-buckling equilibrium is given by [9]

$$\begin{aligned} &\frac{d}{ds}\left(N_b + \frac{M_b}{\rho_o}\right) - \frac{1}{\rho_o}\left(N + \frac{M}{\rho_o}\right)\psi_{o\eta b} - \frac{1}{\rho_o}\left(N_b + \frac{M_b}{\rho_o}\right)\psi_{o\eta b} = 0\,, \\ &\frac{d^2M_b}{ds^2} - \frac{N_b}{\rho_o} - \frac{d}{ds}\left[\left(N + \frac{M}{\rho_o} + N_b + \frac{M_b}{\rho_o}\right)\psi_{o\eta b} + \left(N_b + \frac{M_b}{\rho_o}\right)\psi_{o\eta}\right] = 0, \end{aligned} \tag{10}$$

or equivalently, in terms of the kinematical quantities this set simplifies to

$$\varepsilon_{mb} = \text{constant}\,, \tag{11}$$

$$W_{ob}^{(4)} + (2 + \chi^2 - 1)W_{ob}^{(2)} + \chi^2 W_{ob} = m\varepsilon_{mb}\left[1 - W_o^{(2)} - W_o\right], \quad W_{ob} = w_{ob}/\rho_o. \tag{12}$$

4. SOLUTION FOR THE PRE-BUCKLING STATE

Because all the geometry, the loading and the support conditions are symmetric to $\zeta(\varphi = 0)$, only a half-arch is modelled – see Figure 3. The general solution satisfying equilibrium equation (9) is sought on the right half of the arch in the form

$$W_o = \frac{\chi^2 - 1}{\chi^2} + A_1\cos\varphi + A_2\sin\varphi - \frac{A_3}{\chi^2}\cos\chi\varphi - \frac{A_4}{\chi^2}\sin\chi\varphi\,, \; A_i \in R. \tag{13}$$

The integration constants A_i can be determined by utilizing the boundary conditions gathered in Table 1. At the right support the displacement and the bending moment are zero. At the crown point the rotation is zero and there is a jump in the shear force distribution with magnitude $P_\zeta/2$. Altogether, there are four unknowns and four equations in a linear system. Closed-form solutions are possible. With the normal displacement in hand, the rotation can also be calculated recalling Eq. (1). Since the axial strain is constant on the centroidal axis – see Eq. (8) – one can write

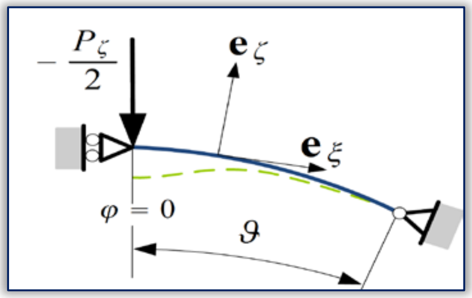

Figure 3: Half-arch model in the pre-buckling state

$$\varepsilon_m = \frac{1}{\vartheta}\int_0^{\vartheta} \varepsilon_m(\varphi)d\varphi = I_1 + I_2\mathbf{P} + I_3\mathbf{P}^2 \tag{14}$$

where $\mathbf{P} = (-P_\zeta\rho_o^2\vartheta)/(2I_{e\eta})$ is a dimensionless load. Constants I_1, I_2, I_3 can be expressed in closed form.

Table 1. Pre-buckling boundary conditions

$W_o^{(1)}\Big\vert_{\varphi=+0} = 0$	$W_o\Big\vert_{\varphi=\vartheta} = 0$
$I_{e\eta}W_o^{(3)}\Big\vert_{\varphi=+0} = \frac{P_\zeta}{2}$	$W_o^{(2)}\Big\vert_{\vartheta} = 0$

5. SOLUTIONS FOR THE BUCKLED EQUILIBRIUM STATE

The general solution of equation (12) takes the form

$$W_{ob} = C_1\cos\varphi + C_2\sin\varphi + C_3\sin(\chi\varphi) + C_4\cos(\chi\varphi) - \frac{m\varepsilon_{mb}}{2\chi^3}\left(\frac{2}{\chi} + A_3\varphi\sin(\chi\varphi) - A_4\varphi\cos(\chi\varphi)\right) \tag{15}$$

while, if the increment ε_{mb} is zero, it simplifies to

$$W_{ob}(\varphi) = D_1\cos\varphi + D_2\sin\varphi + D_3\sin\chi\varphi + D_4\cos\chi\varphi\,; \quad C_i, D_i \in R\,. \tag{16}$$

After buckling, every physical quantity is continuous through the interval $\varphi \in [-\vartheta;\vartheta]$ because there is no increment in the loading.

Possibly, there is symmetric (or limit point) and antisymmetric (or bifurcation) buckling. If the buckled arch shape is [antisymmetric] (symmetric) then [$\varepsilon_{mb} = 0$] ($\varepsilon_{mb} \neq 0$). These possibilities are shown on the [left](right) side in Figure 4. The continuous line represents the centroidal axis of the arch in the initial configuration, the dashed line is the pre-buckling shape while the dotted line is the buckled shape.

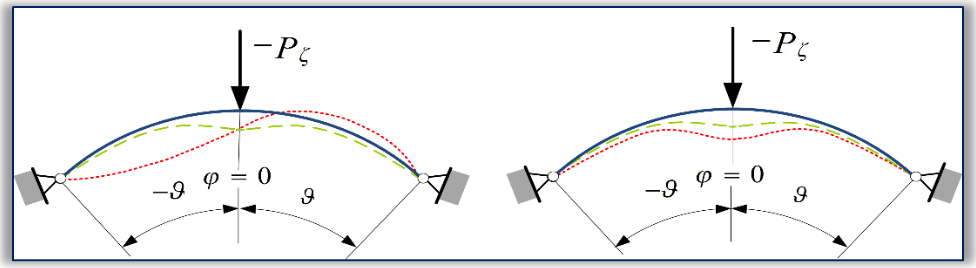

Figure 4: Possible pre-buckling and buckled arch shapes

First let us deal with bifurcation buckling. As all fields are continuous, now the whole arch is considered, consequently the displacement and the bending moment are zero at the end supports. After substituting solution (16) into the boundary conditions (BCs) in Table 2, a homogeneous system of linear equations is found for which nontrivial solution exists if the determinant of the coefficient matrix is set to zero:

$$D = (1-\chi)^2(1+\chi)^2\sin\chi\vartheta\cos\chi\vartheta\cos\vartheta\sin\vartheta = 0\,. \tag{17}$$

Recalling the relation $\chi^2 = 1 - m\varepsilon_m$ the lowest physically possible solution is $\chi = \pi/\vartheta$, thus

$$\varepsilon_{m;\mathtt{crit}} = \frac{1}{m}\left(1-\chi^2\right) = \frac{1}{m}\left[1-\left(\frac{\pi}{\vartheta}\right)^2\right] \tag{18}$$

is the lowest (critical) strain.

Table 2. Boundary conditions for bifurcation buckling

$W_{ob}\big\|_{\varphi=-\vartheta} = 0$	$W_{ob}\big\|_{\varphi=\vartheta} = 0$
$W_{ob}^{(2)}\big\|_{\varphi=-\vartheta} = 0$	$W_{ob}^{(2)}\big\|_{\varphi=\vartheta} = 0$

When dealing with limit point buckling, it is again easier to consider only the right half of the arch. The boundary conditions are presented in Table 3. Upon substitution of solution (15) into the boundary conditions, an inhomogeneous system of equations is found which can be solved in a closed form. With W_{ob} in hand, the rotation increment is $\psi_{o\eta b} = -W_{ob}^{(1)}$, thus, the constant strain increment is

$$\varepsilon_{mb} = \frac{1}{2\vartheta}\int_{-\vartheta}^{\vartheta}\left(U_{ob}^{(1)} + W_{ob} + \psi_{o\eta b}\psi_{o\eta}\right)d\varphi. \tag{19}$$

Observe that $\psi_{o\eta} = -W_o^{(1)}$ is an odd function of φ, consequently if W_{ob} is an odd function of φ then the above integral indeed vanishes for bifurcation buckling: $\varepsilon_{mb} = 0$. Otherwise – practically if W_{ob} is an even function in φ – ε_{mb} is a nonzero constant.

Table 3. Boundary and continuity conditions for limit-point buckling

$W_{ob}^{(1)}\big\|_{\varphi=-\vartheta} = 0$	$W_{ob}\big\|_{\varphi=\vartheta} = 0$
$W_{ob}^{(3)}\big\|_{\varphi=-\vartheta} = 0$	$W_{ob}^{(2)}\big\|_{\varphi=\vartheta} = 0$

Substituting now all the previously determined kinematical quantities into Eq. (19), then performing the integration and simplifying by the constant increment ε_{mb}, it is found that

$$1 = J_1 + J_2\mathbf{P} + J_3\mathbf{P}^2\,, \quad J_i \in R. \tag{20}$$

Here each of the constants J_i can be expressed in a closed form [9].

To find the critical load for bifurcation buckling, the critical strain (18) should be substituted to (14). For limit point buckling, nonlinear equations (14) and (20) have to be solved simultaneously for the two unknowns: critical strain and critical load.

6. THE EFFECT OF MATERIAL COMPOSITION ON THE BUCKLING LOAD

It is now investigated how heterogeneity can affect the buckling load of bi-layered arches with rectangular cross-section, given that only the material composition changes -- the overall geometry remains unchanged. As can be seen from Figure 5, the upper layer has Young's modulus E_1 and height b_1. The height is a parameter: $b_1 \in [0, b]$. When $b_1 = 0$, the arch is homogeneous with Young's modulus E_2. In this case, the heterogeneity parameter is always noted by $m_{\mathbf{hom}}$ and the radius of the E-weighted centroidal axis is $\rho_{o\,\mathbf{hom}}$. If $b_1 = b$, the homogeneous cross-section has Young's modulus E_1. For any other (and obviously heterogeneous) distributions, the notations $m_{\mathbf{het}}$ and $\rho_{o\,\mathbf{het}}$ are used.

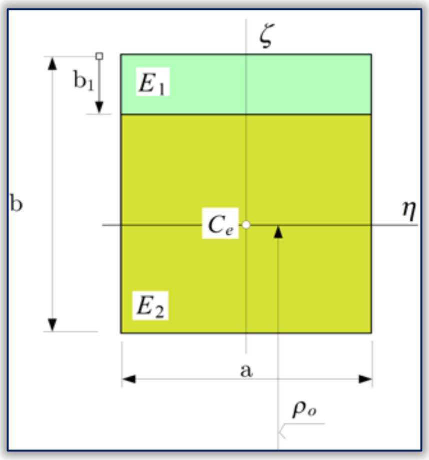

Figure 5: Bi-layered rectangular cross-section

Recalling (4)₃ it is intended to find how the ratio

$$\frac{m_{\mathbf{het}}}{m_{\mathbf{hom}}(b_1 = 0)} = \frac{A_e I_\eta E_2}{A E_2 I_{e\eta}} \left[\frac{\rho_{o\,\mathbf{het}}}{\rho_{o\,\mathbf{hom}}} \right]^2 \tag{21}$$

is related to the material distribution. It turns out that this fraction is a function of the quotients ρ_o / b, b_1 / b and E_2 / E_1 for this simple rectangular cross-section. The first, and otherwise dominant term on the right side of the former expression depends only on the ratios E_2 / E_1 and b_1 / b -- see the definitions (3)-(4). Some solutions are plotted on Figure 6. On the account of heterogeneity, up to a 55% difference can be experienced when $E_2 / E_1 = 5$. It is also clear that when $b / b_1 = 0.5$, the related curves intersect each other and the maxima of these are also the same. It means that the plotted ratio is obviously independent of whether the upper or the lower layer has greater Young's modulus. The quotient E_2 / E_1 only affects at what rate of b / b_1 the maximum is reached.

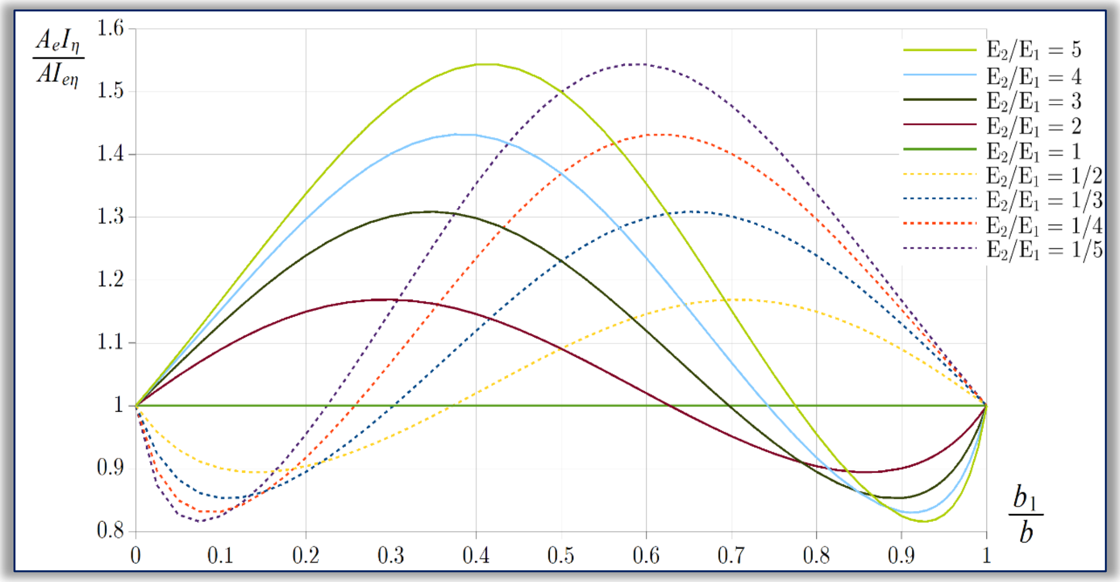

Figure 6: Variation of some material and geometrical parameters

The second term in (21) further depends on the ratio $\rho_{o\,\mathbf{hom}} / b$. For the values 10, 50 and 100, the results are plotted in Figure 7. It can be seen that this term has a much less considerable effect -- at most $\pm 4\%$, when $\rho_{o\,\mathbf{hom}} / b = 10$. For the other two selected ratios it is always less than 1%. So for most geometries and material distributions the ratio $(\rho_{o\,\mathbf{het}} / \rho_{o\,\mathbf{hom}})^2$ can be considered to be 1 with a good accuracy.

To sum up, the ratio $m_{\mathbf{het}} / m_{\mathbf{hom}}$ is always the product of the previous two matching figures. This quotient for $\rho_{o\,\mathbf{hom}} / b = 10$ is plotted in Figure 8. The maximum value is a considerable 1.589.

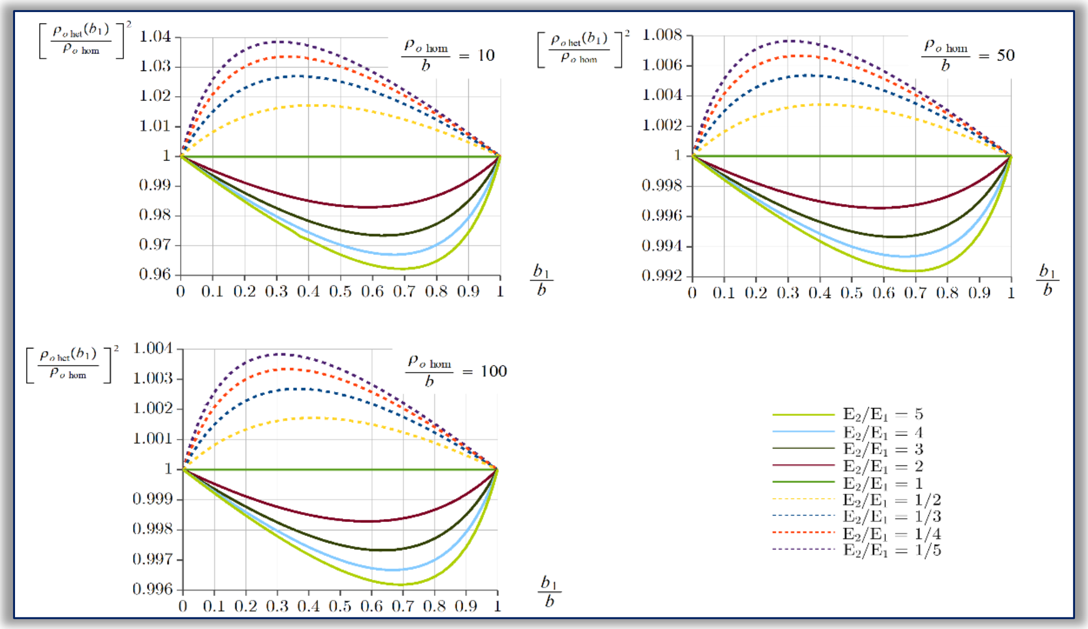

Figure 7: Variation of some typical parameters

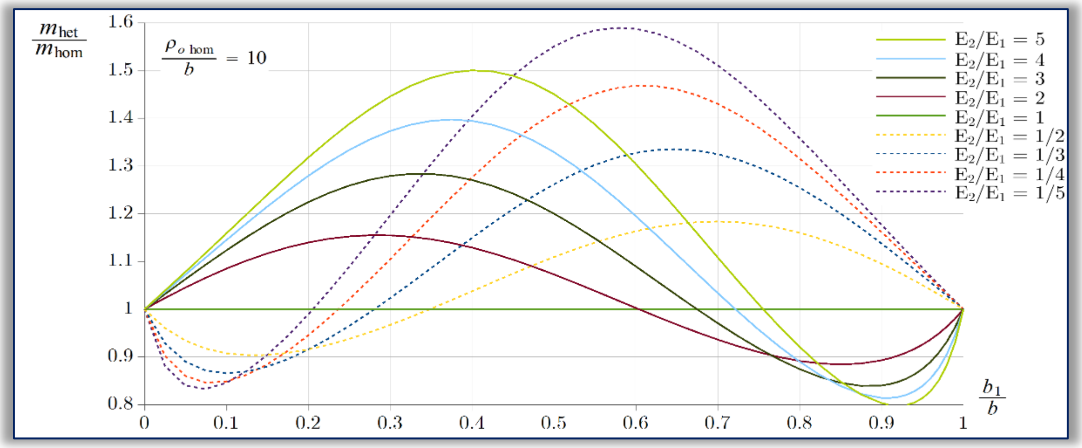

Figure 8: Possible values for parameter m for various distributions

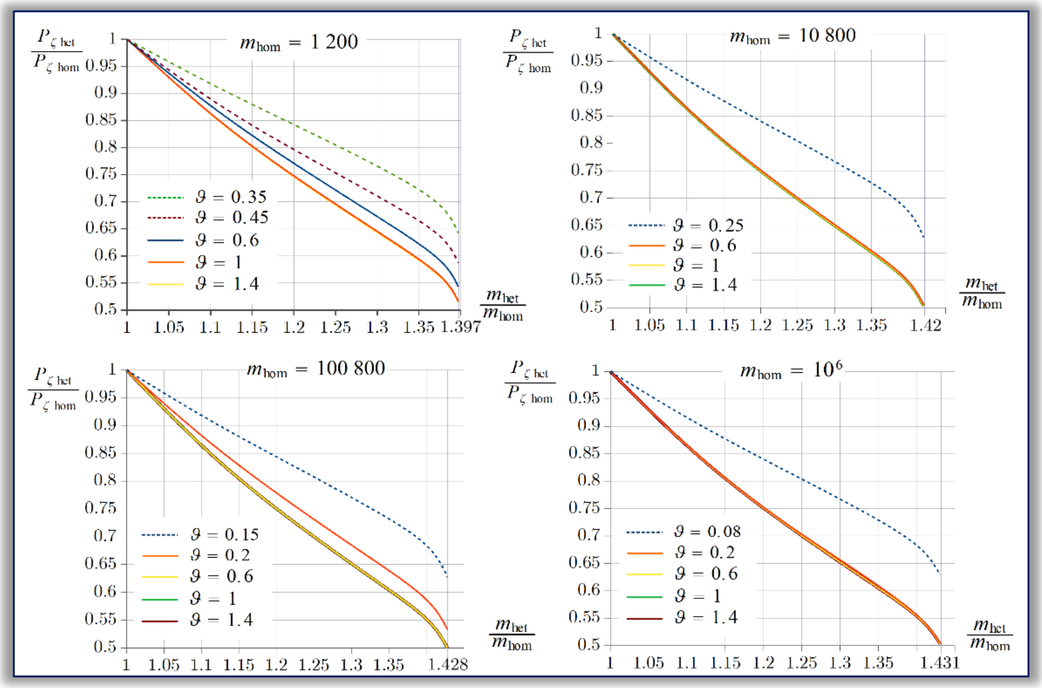

Figure 9: Change in the lowest buckling load due to various parameters

Let us see now tackle some numerical examples. A circular arch with $E_2/E_1 = 4$ is chosen. The following $m_{\mathbf{hom}}$ values are selected: $\{1.2\cdot 10^3;\ 1.08\cdot 10^4;\ 1.0008\cdot 10^5;\ 10^6\}$. It is intended to find how heterogeneity affects the critical load through the variation of the parameter m. Investigations are carried out until the maxima of the parameter $m_{\mathbf{het}}$ is reached, while gradually increasing the ratio b_1/b -- see the preceding figures. All the results are shown graphically in Figure 9. For every selected included angle only the dominant buckling mode (either bifurcation or limit-point) is evaluated. When the buckled arch shape is symmetric, the corresponding curve is dashed. When it is antisymmetric (it is the more general for pinned supports), then the curve is continuous.

7. CONCLUSIONS

Overall, it can concluded that heterogeneity has a really considerable effect on the buckling load, independently of the magnitude of the selected m parameter values. This can be up to 50% for antisymmetric case and 41% for symmetric buckling. It is also a conclusion that, the semi-vertex angle ϑ does not really have an impact on the plotted ratios: the related curves usually coincide in the majority of the interval. On Figure 9, it can as well be observed that increasing the value of $m_{\mathbf{hom}}$ results a slight increase in the maxima of the ratio $m_{\mathbf{het}}/m_{\mathbf{hom}}$ measured along the abscissa.

Acknowledgements

This research was supported by the National Research, Development and Innovation Office -- NKFIH, K115701.

References

[1] D. Gönczi: Thermal stresses in thin anisotropic hollow circular disk. Annals of Faculty of Engineering Hunedoara – International Journal of Engineering. 14(2), 59-64, 2016.
[2] D. Gönczi: Thermoelastic analysis of thick-walled functionally graded spherical pressure vessels with temperature-dependent material properties. Journal of Computational and Applied Mechanics. 12(2), 109-125, 2017.
[3] Y. L. Pi, M. A. Bradford, and B. Uy: In-plane stability of arches. International Journal of Solids and Structures, 39,105–125, 2002.
[4] B. Uy M. A. Bradford and Y-L. Pi. In-plane elastic stability of arches under a central concentrated load. Journal of Engineering Mechanics, 128(7), 710–719, 2002.
[5] S. t. Yan, X. Shen, Z. Chen, and Z. Jin: On buckling of non-uniform shallow arch under a central concentrated load. International Journal of Mechanical Sciences, 133, 330–343, 2017.
[6] S. t. Yan, X. Shen, Z. Chen, and Z. Jin: Collapse behavior of non-uniform shallow arch under a concentrated load for fixed and pinned boundary conditions. International Journal of Mechanical Sciences, 137, 46–67, 2018.
[7] M. Bateni; M. R. Eslami: Non-linear in-plane stability analysis of FG circular shallow arches under uniform radial pressure. Thin Walled Structures, 94, 302–313, 2015.
[8] M. Bateni, M. R. Eslami: Non-linear in-plane stability analysis of FGM circular shallow arches under central concentrated force. International Journal of Nonlinear Mechanics. 60, 58–69, 2014.
[9] L. Kiss, G. Szeidl: Nonlinear in-plane stability of heterogeneous curved beams under a concentrated radial load at the Crown Point. Technische Mechanik. 35(1), 1-30, 2015.
[10] L. Kiss, G. Szeidl: In-plane stability of fixed-fixed heterogeneous curved beams under a concentrated radial load at the Crown Point. Technische Mechanik. 35(1), 31-48, 2015.
[11] L. P. Kiss: Vibrations and stability of heterogeneous curved beams. Ph.D. thesis, Institute of Applied Mechanics, University of Miskolc, Hungary, 2015.

ISSN 1584 - 2665 (printed version); ISSN 2601 - 2332 (online); ISSN-L 1584 - 2665